IEEE Photonics Journal
An IEEE Photonics Society Publication

Open Access

Anisotropic-Material-Induced Rotation of Field Distribution in Circular Plasmonic Resonator

Volume 11, Number 1, February 2019

Xiaokang Song
Shilei Li
Yuanyuan Chen
Yinxing Ding
Gaoyan Duan
Lulu Wang
Li Yu

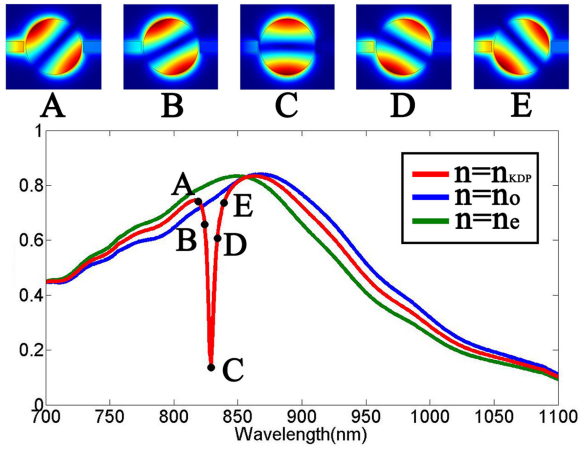

DOI: 10.1109/JPHOT.2018.2884761
1943-0655 © 2018 IEEE

IEEE photonics SOCIETY

IEEE

Anisotropic-Material-Induced Rotation of Field Distribution in Circular Plasmonic Resonator

Xiaokang Song,[1,2] **Shilei Li**,[1,2] **Yuanyuan Chen**,[3] **Yinxing Ding**,[1,2] **Gaoyan Duan**,[1,2] **Lulu Wang**,[1,2] **and Li Yu** [1,2]

[1]State Key Laboratory of Information Photonics and Optical Communications, Beijing University of Posts and Telecommunications, Beijing 100876, China
[2]School of Science, Beijing University of Posts and Telecommunications, Beijing 100876, China
[3]China South Industries Research Academy, Beijing 100089, China

DOI:10.1109/JPHOT.2018.2884761

Manuscript received August 19, 2018; revised October 29, 2018; accepted November 28, 2018. Date of publication December 3, 2018; date of current version December 28, 2018. This work was supported by the National Natural Science Foundation of China under Grants 11574035, 11604020, and 11404030.
Corresponding author: Li Yu (e-mail: yuliyuli@bupt.edu.cn).

Abstract: A metal–insulator–metal plasmonic structure that contains a circular cavity with anisotropic material (AM) is designed and numerically simulated. Attributed to filling the cavity with AM, the standing wave patterns in the cavity rotate clockwise as the wavelength increases, resulting in a new valley on the transmission spectrum, which will not appear in the isotropic-material case. In order to understand the underlying physical mechanism of the phenomena, the influences of the parameters of AM, such as optical axis angle and refractive indexes, on transmission spectrum were investigated. All results can be explained well by the index ellipsoid method and the coupled mode theory. This work shows the unique role of AM in the plasmonics nanostructure and these phenomena may have potential applications in the nanoscale integrated photonic circuits.

Index Terms: Surface plasmons, anisotropic, interference, integrated optics.

1. Introduction

Surface plasmon polaritons (SPPs), which have been studied in recent years for their ability of overcoming the diffraction limit of light, can confine and propagate the electromagnetic at a subwavelength scale. Because of their superior characteristic, SPPs are regarded as a promising candidate to realize the nanoscale integrated photonic circuits [1], [2]. Various nanostructures based on SPPs have been proposed and investigated, such as metallic nanowires and films [3]–[5], V grooves in metal substrates [6], hybrid SPPs waveguide [7], etc. Among these structures, metal-insulator-metal (MIM) waveguides, in particular, can strongly confine the SPPs in the insulator region and SPPs in MIM waveguide have acceptable propagation length [8], [9]. Thus, a variety of functional plasmonic structures based on MIM wavelength are designed, such as filers [10]–[12], ring resonators [13], splitters [14], and demultiplexers [15]–[17]. Various materials are used in these structures to implement different functions, e.g., semiconductor [18] and gain material [19]. However, these structures based on anisotropic material (AM) have hardly been discussed, while MIM waveguides with the AM have been investigated [20]. It is meaningful to study the SPPs in MIM plasmonic structure with

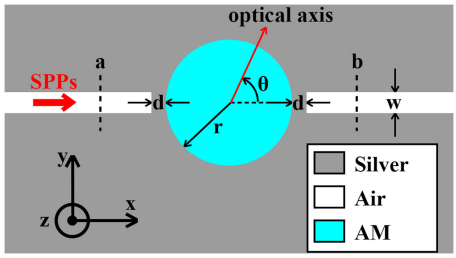

Fig. 1. Schematic diagram of the proposed plasmonic resonator system that composed of a MIM waveguide and a circular cavity filled with AM.

AM, because many materials, such as some nonlinear materials, are anisotropic, which may be used in the integrated photonic [21].

In this paper, a MIM plasmonic structure consisting of circular cavity filled with AM is proposed and investigated. Duo to the AM in the circular cavity, the standing wave patterns in the cavity rotate clockwise as the wavelength increases. The rotation affects the out-coupling strength between the cavity and MIM waveguide, resulting in a valley on the transmission spectrum. The simulation results also show that the characteristics of AM, e.g., angle of optical axis, refractive indexes of ordinary light (n_o) and extraordinary light (n_e), can affect the peak and valley of the transmittance spectrum. The increase of optical axis angle can induce the red shift of the valley and blue shift of the peak, and the refractive indexes of AM determine the depth and width of the valley. In addition, the influence of coupling distance between the cavity and waveguide on the spectrum has also been investigated. All the above results can be explained by the index ellipsoid method and the coupled mode theory. The analysis shows that the two specific components of the AM permittivity tensor have influence on the field distribution in the cavity, which leads to the rotation of standing wave patterns. The research may provide a route to control the SPPs and find important applications in the nanoscale optical device.

2. Design and Method

Fig. 1 shows the two-dimensional geometry of the plasmoic resonator system that composed of a MIM waveguide and a circular cavity filled with AM. Because the circular cavity is the simplest centrosymmetric structure, it is convenient to show the impact of AM [22], [23]. The width w of the MIM waveguide is fixed to 50 nm. r is the radius of the circular cavity. The coupling distance between circular cavity and waveguide is set as $d = 10$ nm. θ is the angle between horizontal direction and the optical axis of AM. The metal of structure is assumed to be silver (Ag, shaded gray). The dielectric of waveguide is air (shaded white). The AM filled in circular cavity is assumed to be KH_2PO_4 (KDP) [24], which is a common AM. The permittivity of Ag and KDP as function of wavelength (λ) was taken from the literatures [25] and [24], respectively, and expanded using the method of interpolation. Especially, KDP has two refractive indexes of n_o and n, they are expanded respectively.

As we all know, the permittivity of AM is a second order tensor and determined as follows when the optical axis is parallel to axis [20]:

$$\varepsilon = \begin{bmatrix} n_x^2 & 0 & 0 \\ 0 & n_y^2 & 0 \\ 0 & 0 & n_z^2 \end{bmatrix} \tag{1}$$

where we assume that the optical axis is parallel to x axis, n_x, n_y and n_z are refractive indexes of AM in the x y z axis, respectively. Assuming that the optical axis is misaligned from the waveguide

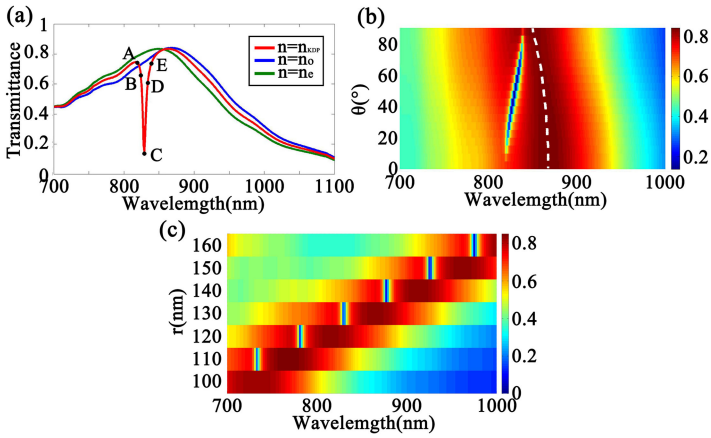

Fig. 2. (a) Transmission spectrums of the structure filled with isotropy material of which refractive index n $= n_o$ (blue line) and n $= n_e$ (green line) and AM of which refractive index n $= n_{KDP}$ (red line), respectively. (b) Transmission spectra of the structure filled with KDP with the angle θ increasing from 0° to 90° and the peak line of the transmission spectra (white dash line). (c) Transmission spectra of the structure filled with KDP as the radius of the cavity increases from 100 nm to 160 nm.

axes by the angle θ in the *x* - *y* plane as shown in Fig. 1, the permittivity tensor becomes [20]:

$$\varepsilon' = \begin{bmatrix} \cos^2\theta n_x^2 + \sin^2\theta n_y^2 & \sin\theta\cos\theta(n_y^2 - n_x^2) & 0 \\ \sin\theta\cos\theta(n_y^2 - n_x^2) & \sin^2\theta n_x^2 + \cos^2\theta n_y^2 & 0 \\ 0 & 0 & n_z^2 \end{bmatrix} = \begin{bmatrix} \varepsilon_{11} & \varepsilon_{12} & 0 \\ \varepsilon_{21} & \varepsilon_{22} & 0 \\ 0 & 0 & \varepsilon_{33} \end{bmatrix}$$

$$\begin{aligned} \varepsilon_{11} &= \cos^2\theta n_x^2 + \sin^2\theta n_y^2 \\ \varepsilon_{12} &= \varepsilon_{21} = \sin\theta\cos\theta(n_y^2 - n_x^2) \\ \varepsilon_{22} &= \sin^2\theta n_x^2 + \cos^2\theta n_y^2 \\ \varepsilon_{33} &= n_z^2 \end{aligned} \tag{2}$$

In the simulation, we assume that n_x and n_y are equal to n_e and n_o of KDP, respectively. Because the structure is a two-dimensional model and SPPs can only exist for TM polarization [26], n_z has no effect on the results and is neglected in the simulations.

The transmittance spectrum of the structure is calculated by the finite-element method (FEM) of COMSOL Multiphysics. In the simulation, the transmittance of SPPs at port b is defined as quotient between the SPPs power flows of port b and port a. Only the fundamental TM mode is excited in the structure and propagates from left to right. Ohmic losses of plasmonic have great influence on the SPPs transmission in practical applications. Therefore, we calculated propagation length of SPPs in the waveguide. The effective propagation length of SPPs is defined as *L*spps $= 1 / [2\mathrm{Im}(\beta)]$ [26]. β is the wave vector in the direction of propagation. The result shows that the propagation length is longer than 16.65 μm when wavelength is larger than 700 nm, which includes the wavelength range we use. This is much longer than the size of our structure. Therefore, ohmic losses can be ignored in our structure and it will not have too much influence on experimental attempt.

3. Simulation and Discussion

Fig. 2(a) shows the transmission spectra of the structure that is filled with different materials. The radius of the cavity is set as $r = 130$ nm. The red line in Fig. 2(a) is the spectrum of the structure filled with KDP. And the angle θ of KDP is 45°. The blue and green lines in Fig. 2(a) are the spectra of the structure filled with isotropic material. n_o and n_e are the refractive indexes of isotropic material

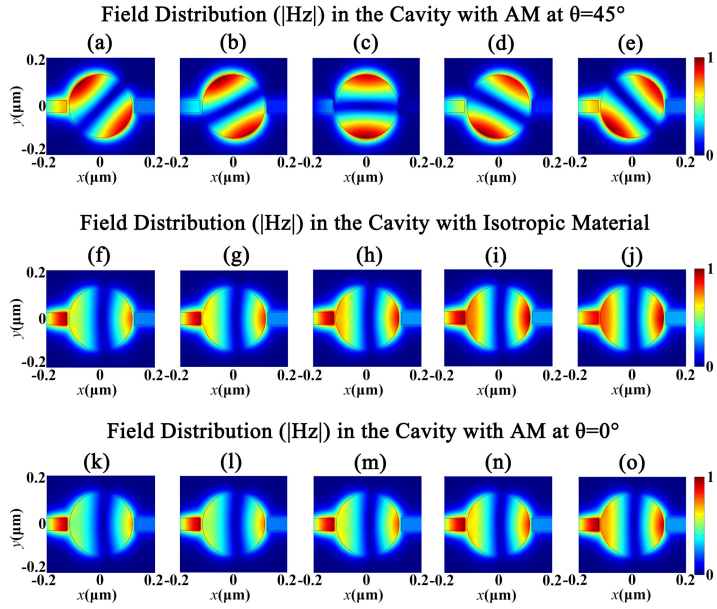

Fig. 3. (a)–(e) Normalized field distribution of |Hz| in circular cavity filled with KDP at $\theta = 45°$ at (a) $\lambda = 819$ nm, (b) $\lambda = 824$ nm, (c) $\lambda = 829$ nm, (d) $\lambda = 834$ nm, (e) $\lambda = 839$ nm. (f)–(j) Normalized field distribution (|Hz|) in circular cavity filled with isotropic material of which value of the index is equal to n_e of KDP at (f) $\lambda = 819$ nm, (g) $\lambda = 824$ nm, (h) $\lambda = 829$ nm, (i) $\lambda = 834$ nm, (j) $\lambda = 839$ nm. (k)–(o) Normalized field distribution (|Hz|) in circular cavity filled with KDP at $\theta = 0°$ at (k) $\lambda = 810$ nm, (l) $\lambda = 815$ nm, (m) $\lambda = 820$ nm, (n) $\lambda = 825$ nm, (o) $\lambda = 830$ nm.

in blue line and green line, respectively. These three lines all have nearly symmetric Lorentzian-like line-shape with resonant wavelength of 849 nm (green line), 863 nm (red line) and 868 nm (blue line). It means that the effective index of the cavity filled with KDP (red line) is equal to a value between n_o (blue line) and n_e (green line) at resonance wavelength, since the resonant wavelength of the red line is between the green and blue lines. And the biggest different between the red line and the other lines is that a valley appears on the red line. The wavelength of the valley is around 829 nm. Fig. 2(b) shows the transmission spectra of the structure filled with KDP at different angle θ. The angle θ increases from 0° to 90° [bottom to top in Fig. 2(b)] with an interval of 5°. In Fig. 2(b), the *x* axis and *y* axis represent the wavelength λ and angle θ, respectively. One can find that the peak blue shifts [white dash line in Fig. 2(b)] and the valley red shifts as the angle θ increases. Simultaneously, the valley disappears at $\theta = 0°$ and 90° and reaches its minimum at $\theta = 45°$. Fig. 2(c) shows the transmission spectra with different *r* at $\theta = 45°$. *r* increases from 100 nm to 160 nm [bottom to top in Fig. 2(c)] with an interval of 10 nm. The *x* axis and *y* axis represent the wavelength λ and radius *r*, respectively. In Fig. 2(c), it is obvious that the spectra red shift with *r* increasing from 100 nm to 160 nm and there is no change in the line-shape of the spectra.

To understand origin of the valley, the field distributions ($|H_z|$) in circular cavity are calculated and displayed in Fig. 3(a)–(e) with $\theta = 45°$ at wavelength of 819 nm, 824 nm, 829 nm, 834 nm and 839 nm. The point A-E on the red line of Fig. 2(a) corresponds to the Fig. 3(a)–(e), respectively. It is clearly observed that the field distribution patterns rotate clockwise as the wavelength increases. In Fig. 3(c) that is the field distributions of the valley, the standing wave resonates in the *y* direction and field is confined in the bottom and top of the cavity, which leads to almost no field existing in the middle part of cavity. Therefore, field cannot couple into right waveguide, resulting in the valley on the red line. The rotation of field distribution won't appear in the isotropic material cavity as shown in Fig. 3(f)–(j), which is the field distributions of blue line at the same wavelengths as Fig. 3(a)–(e). And the field distributions of green line are similar to the blue line which is not shown in the figure. According to that, the rotation of the field distribution is related to the anisotropy of KDP, which will be discussed next.

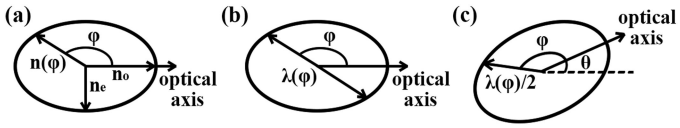

Fig. 4. (a) Schematic diagram of the index ellipsoid. (b) Schematic diagram of the dependence of resonant wavelength λ and angle φ in the circular cavity. (c) Schematic diagram of making the optical axis of (b) deviate from the *x* axis by θ.

The refractive index of anisotropic crystals can be expressed by a geometrical method called refractive index ellipsoid, which is displayed in Fig. 4(a) [27]. n_o and n_e are semi-major and semi-minor axes of the refractive index ellipsoid, respectively. $n(\varphi)$ is the effective refractive index of wave in the propagation direction. Its value equals the distance from center to edge of ellipsoid at φ. φ is the angle between the optical axis and the propagation direction of wave. The refractive index ellipsoid clearly expresses the different effective indexes of wave at different propagation direction. By the geometric method, $n(\varphi)$ can be expressed as follows [27]:

$$n(\varphi) = \frac{n_o n_e}{\sqrt{\sin^2(\varphi) n_o^2 + \cos^2(\varphi) n_e^2}} \tag{3}$$

The cavity in Fig. 1 is a round with radius *r*. Therefore, the resonant wavelength of the circular cavity filled with KDP is determined as follows [28]:

$$\lambda(\varphi) = \frac{2 \times 2(r + \Delta r) n(\varphi)}{m} = 4(r + \Delta r) n(\varphi) = \frac{4 n_o n_e (r + \Delta r)}{\sqrt{\sin^2(\varphi) n_o^2 + \cos^2(\varphi) n_e^2}} \tag{4}$$

where Δr is correction term of *r*. Because the circular cavity is not a standard Fabry-Perot (FP) resonator, *r* is not exactly the same as the length of FP resonator. The positive integer *m* is the number of antinodes of the standing waves, which equals 1 according to the Fig. 3(a)–(e). The schematic diagram of $\lambda(\varphi)$ is shown in Fig. 4(b). The Eq. (4) shows that the direction of the standing wave depends on wavelength, which results in rotation of the field distribution as shown in Fig. 3(a)–(e). From Eq. (4), it can also be known that resonant wavelength $\lambda(\varphi)$ is proportional to the radius *r*, which is consistent with Fig. 2(c). Fig. 4(c) shows the schematic diagram of the index ellipsoid after the optical axis is misaligned from *x* axis by θ. Therefore, the angle between *x* axis and direction of the standing waves equals $\varphi + \theta$. Because the direction of standing wave is parallel to *y* axis for the valley, one can get $\varphi + \theta = 90°$. Considering $\varphi = 90° - \theta$ and Eq. (4), the resonant wavelength of valley can be written as:

$$\lambda_{\text{valley}} = \lambda(90^\circ - \theta) = \frac{4 n_o n_e (r + \Delta r)}{\sqrt{\sin^2(90^\circ - \theta) n_o^2 + \cos^2(90^\circ - \theta) n_e^2}} = \frac{4 n_o n_e (r + \Delta r)}{\sqrt{\cos^2(\theta) n_o^2 + \sin^2(\theta) n_e^2}} \tag{5}$$

The resonant wavelengths of the valley at different θ are displayed in Fig. 5(a) (green point). A good fitting between Eq. (5) and the point has been achieved by using fitting parameter of $\Delta r = 9.8986$ nm and the result is shown in Fig. 5(a) (blue line). In the fitting, $n_o = 1.5006$ and $n_e = 1.4629$ are used, which are average values of refractive indexes at wavelength range from 819 nm to 839 nm. Fig. 5(a) also shows some mismatch between the fitting and the data points at small and large wavelengths. This slight deviation is due to the dispersion of n_o, n_e and Δr, which are not included in the model. In the fitting, n_o and n_e are fixed values, and they are approximately the same as values of refractive indexes near center wavelength (829 nm). Simultaneously, they have some difference with the refractive indexes of large and small wavelengths. Therefore, the fitting is better near center wavelengths and worse at small and large wavelengths. In addition, because Δr is affected by the refractive index and should have dispersion, it may also cause some mismatch in the fitting results, which is similar to the effect of refractive index on the fitting.

In addition, the peak of spectrum can also be explained by Eq. (4). Since the standing wave parallel to *x* axis for the peak, the angle between *x* axis and direction of the standing wave is $\varphi + \theta$

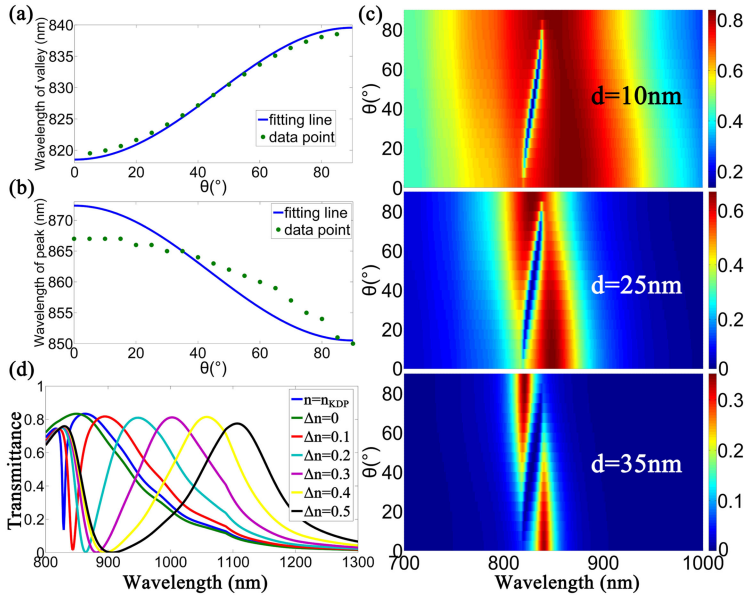

Fig. 5. (a) Dependence of the resonant wavelength of valley and angle θ (green point), and the fitting line (blue line) of the points. (b) Dependence of the resonant wavelength of peak and angle θ (green point), and the fitting line (blue line) of the points. (c) Transmission spectra of the structure filled with KDP with the angle θ increasing from 0° to 90° at coupling distance d = 10 nm, 25 nm and 35 nm. (d) Transmission spectra with different Δn from 0 to 0.5 (corresponding to green, red, cyan, purple, yellow and black lines, respectively), blue line is the transmission spectrum of KDP.

= 0°, which means $\varphi = -\theta$. Therefore, the resonant wavelength of the peak can be expressed as:

$$\lambda_{peak} = \lambda(-\theta) = \frac{4n_o n_e(r+\Delta r)}{\sqrt{\sin^2(-\theta)n_o^2 + \cos^2(-\theta)n_e^2}} = \frac{4n_o n_e(r+\Delta r)}{\sqrt{\sin^2(\theta)n_o^2 + \cos^2(\theta)n_e^2}} \tag{6}$$

Contrasting Eqs. (5) and (6), it is noted that denominators of them are different. Because n_o is larger than n_e for KDP, the denominator of Eq. (5) decreases and the denominator of Eq. (6) increases with θ increasing from 0° to 90°. This is the reason that the peak blue shifts and the valley red shifts with increase of θ in Fig. 2(b). However, the fitting between Eq. (6) and the points of peak is not very well as shown in Fig. 5(b). To understand the origin of deviation in the fitting, the difference between the field distribution of peak and valley is investigated. Comparing the field distribution of peak and valley, it is noted that there are waveguides on both sides of the circular cavity and the field distribution of the peak is confined to same sides. Therefore, the waveguides are considered to have influence on the distribution field of the peak. In order to verify it, the transmittance spectra of the structure with different coupling distance d are simulated and shown in Fig. 5(c). In Fig. 5(c), there are three 2-dimensional figures of the transmittance spectra with d = 10 nm, 25 nm and 35 nm. The angle θ of optical axis in each figure increases from 0° to 90° with an interval of 5°. As can be seen from Fig. 5(c), the peak become narrow and maximum of spectrum become small [according to the color bar in Fig. 5(c)] with coupling distance increasing, which can be explained by coupled mode theory. According to the coupled mode theory, the transmission of the band-pass filter structure can be expressed as [23]:

$$T(\omega) = \frac{(1/\tau_\omega)^2}{(\omega-\omega_0)^2 + (1/\tau_i + 1/\tau_\omega)^2} \tag{7}$$

where ω is the frequency of the incident light and ω_0 is resonance frequency of cavity. τ_ω is the decay rate of the field in the cavity due to the power escapes through the waveguide and τ_i is the decay rate due to the internal loss in the cavity. Since τ_ω increases with the increase of coupling

distance *d*, according to Eq. (7), the transmission $T(\omega)$ become narrow and the maximum of $T(\omega)$ become small, which can explain the above phenomena. In addition, it can be found that the peak of spectra blue shifts with coupling distance increasing in Fig. 5(c). According to the Eq. (5) and Eq. (6), the resonant wavelength of the valley λ_{valley} equals the resonant wavelength of the peak λ_{peak} when $\theta = 45°$. So, the blue shift of the peak demonstrates that the resonant wavelength of peak is closer to the theory results of Eq. (6) with increase of coupling distance *d*. Moreover, it is clearly observed that the valley has no significant change with the increase of coupling distance. It is because that the field distribution of the valley is confined to the upper and lower sides of the cavity, and will not be affected by the waveguides. Therefore, all the above results verified that the waveguides have influence on the resonant wavelength of the peak, which is a main reason that Eq. (6) is not agree well with the simulation results of the peak. And it should also be noted that the peak is cut off by the valley because the peak blue shifts with the increase of *d*. As a result, the resonant wavelengths of the peak around the intersection are not available. Therefore, the good fitting between Eq. (6) and the points of peak still cannot be achieved with weakening the influence of the waveguide.

In Figs. 2(b) and 5(c), the valley disappears at $\theta = 0°$ and 90° and reaches its minimum at $\theta = 45°$. The change in permittivity is considered to be the origin for the phenomenon of the valley. According to Eq. (2), when θ equals 0° or 90°, it can be obtained that $|\varepsilon_{12}| = |\varepsilon_{21}| = 0$ and Eq. (2) changes back to Eq. (1), so that different components of the electric field no longer directly interact with each other. As a result, standing wave can only resonate in the incident direction and the valley disappears at $\theta = 0°$ and 90°. In order to demonstrates this, the field distributions with $\theta = 0°$ and 90° at different wavelength are simulated [An example of $\theta = 0°$ is shown in Fig. 3(k)–(o)]. It matches our expectation that the rotation of field distribution disappeared, which is the reason for appearance of the valley. Conversely, when θ equals 45°, $|\varepsilon_{12}|$ and $|\varepsilon_{21}|$ reach their maximum. Therefore, the valley reaches its minimum at $\theta = 45°$. Comparing to previous work [20], [29], it can be seen that the interaction of different component fields induced by AM in cavity is stronger than it in waveguide. Because the cavity can satisfy resonant condition of wave that waveguide can't satisfy, and resonant characteristics, such as resonant wavelength and field distribution, is sensitive to the refractive index. Therefore, the cavity can better enhance the influence of AM on SPPs than waveguide.

According to the Eq. (5), it can be seen that the maximum and minimum values of the resonant wavelengths in the circular cavity are determined by n_o and n_e, respectively. It means that the difference Δn between n_o and n_e can affect the width of the valley. The spectra with different Δn are simulated and shown in Fig. 5(d). Here, we set $n_o = n_e + \Delta n$ with $\Delta n = 0$, 0.1, 0.2, 0.3, 0.4, and 0.5. n_e is extraordinary light refractive index of KDP. All of spectra are simulated with $\theta = 45°$. The blue line is the spectrum of KDP and the other lines are spectra of $\Delta n = 0$, 0.1, 0.2, 0.3, 0.4, and 0.5 (corresponding to green, red, cyan, purple, yellow and black lines, respectively). It is noted that $\Delta n = 0$ means that the green line is the spectrum of isotropic material with refractive index value equaling n_e.

From Fig. 5(d), obviously, the width and the depth of the valley increase with the increase of Δn. According to Eq. (2), $|\varepsilon_{12}|$ and $|\varepsilon_{21}|$ increase with the increase of Δn. And the magnitude of $|\varepsilon_{12}|$ and $|\varepsilon_{21}|$ determines the depth of the valley, which has been discussed above. Therefore, Δn is proportional to the depth of the valley. In addition, the resonant wavelength of the valley red shifts with Δn increasing in Fig. 5(d). In order to explain this phenomenon, we replace the n_o in Eq. (5) with $\Delta n + n_e$ and differentiate the equation on Δn as follows:

$$\frac{d\lambda(\theta)}{d\Delta n} = \frac{4(r + \Delta r)\sin^2(\theta) n_e^3}{\sqrt{\left(\cos^2(\theta)(n_e + \Delta n)^2 + \sin^2(\theta) n_e^2\right)^3}} \tag{8}$$

The value of Eq. (8) is always greater than 0, so the resonant wavelength of the valley always increases with Δn increasing. Eq. (8) also shows that the resonant wavelength of the valley increases fast when Δn is small, and increases slowly when Δn is large, which is in good agreement with Fig. 5(d). Due to the electro-optic effect of some AMs, the Δn can be dynamically tunable.

Therefore, the above results show a route to change the line type of spectrum without changing the nanostructure.

According to the characteristics of the above spectra, it can be found that the structure with AM may have many potential applications in the nanoscale integrated photonic circuits. For example, considering the characteristic that direction of standing wave pattern is determined by wavelength, a demultiplexers can be achieved by adding multiple out-coupling waveguide to the left of the cavity. Due to the permittivity characteristic of AM, the circular cavity can satisfy the resonant conditions of different wavelengths in different direction. Therefore, compared to the previous work [15]–[17], the structure with AM can reduce the number of resonators and improve the integration of the device. In addition, some of AM belong to the electro-optic materials and $\triangle$n of them can become dynamically tunable by the electro-optic effect. Based on that, the width, depth and resonant wavelength of the valley can be dynamically adjusted, which may be used in devices, such as optical switch, electro-optic modulator and tunable filter. For example, by adjusting the voltage that is applied to the electro-optic materials filled in cavity, we can increase $\triangle$n from zero, so that the transmittance at resonant wavelength of the valley will decrease to zero, which may realize the function of the optical switch and electro-optic modulator. It can be seen that using the electro-optic effect and anisotropy of materials, we have a new way to dynamically control SPPs. And in applications, nematic liquid crystal is a potential AM because it is dynamically tunable and easy to fill in the nanostructure, which we will investigate in the future work.

4. Conclusion

In summary, a plasmonic structure based on MIM with AM has been proposed and investigated. The simulations show that a valley appear on the spectrum due to filling the circular cavity with AM, which will not appear in the case of isotropic material. By analyzing the field distribution of the structure, it is found that the standing wave pattern rotates clockwise as the wavelength increases. These phenomena can be explained by the refractive index ellipsoid. And this method can also explain other changes of the spectra induced by AM, such as the blue shift of peak and the red shift of valley. Moreover, the influence of $\triangle$n on the valley has also been discussed. According to the results above, AM may have many potential applications in the nanoscale integrated photonic circuits, and give an idea to design the functional device, such as demultiplexers, optical switch and electro-optic modulator.

References

[1] W. L. Barnes, A. Dereux, and T. W. Ebbesen, "Surface plasmon subwavelength optics," *Nature*, vol. 424, pp. 824–830, 2003.
[2] L. Liu, Z. Han, and S. He, "Novel surface plasmon waveguide for high integration," *Opt. Exp.*, vol. 13, no. 17, pp. 6645–6650, 2005.
[3] H. Ditlbacher *et al.*, "Silver nanowires as surface plasmon resonators," *Phys. Rev. Lett.*, vol. 95, 2005, Art. no. 257403.
[4] K. Leosson, T. Nikolajsen, A. Boltasseva, and S. I. Bozhevolnyi, "Long-range surface plasmon polariton nanowire waveguides for device applications," *Opt. Exp.*, vol. 14, no. 1, pp. 314–319, 2006.
[5] P. Berini, "Plasmon-polariton waves guided by thin lossy metal films of finite width: Bound modes of symmetric structures," *Phys. Rev. B*, vol. 61, no. 15, pp. 10484–10503, 2000.
[6] S. I. Bozhevolnyi, V. S. Volkov, E. Devaux, and T. W. Ebbesen, "Channel plasmon-polariton guiding by subwavelength metal grooves," *Phys. Rev. Lett.*, vol. 95, 2005, Art. no. 046802.
[7] R. F. Oulton, V. J. Sorger, D. A. Genov, D. F. P. Pile, and X. Zhang, "A hybrid plasmonic waveguide for subwavelength confinement and long-range propagation," *Nature Photon.*, vol. 2, pp. 496–500, 2008.
[8] D. K. Gramotnev and S. I. Bozhevolnyi, "Plasmonics beyond the diffraction limit," *Nature Photon.*, vol. 4, pp. 83–91, 2010.
[9] E. N. Economou, "Surface plasmons in thin films," *Phys. Rev.*, vol. 182, no. 2, pp. 539–554, 1969.
[10] X. Lin and X. Huang, "Tooth-shaped plasmonic waveguide filters with nanometeric sizes," *Opt. Lett.*, vol. 33, no. 23, pp. 2874–2876, 2008.
[11] Y. Matsuzaki, T. Okamoto, M. Haraguchi, M. Fukui, and M. Nakagaki, "Characteristics of gap plasmon waveguide with stub structures," *Opt. Exp.*, vol. 16, no. 21, pp. 16314–16325, 2008.
[12] H. Lu, X. Liu, D. Mao, L. Wang, and Y. Gong, "Tunable band-pass plasmonic waveguide filters with nanodisk resonators," *Opt. Exp.*, vol. 18, no. 17, pp. 17922–17927, 2010.

[13] T. Wang, X. Wen, C. Yin, and H. Wang, "The transmission characteristics of surface plasmon polaritons in ring resonator," *Opt. Exp.*, vol. 17, no. 26, pp. 24096–24101, 2009.
[14] Y. Guo *et al.*, "A plasmonic splitter based on slot cavity," *Opt. Exp.*, vol. 19, no. 15, pp. 13831–13838, 2011.
[15] F. Hu, H. Yi, and Z. Zhou, "Wavelength demultiplexing structure based on arrayed plasmonic slot cavities," *Opt. Lett.*, vol. 36 no. 8, pp. 1500–1502, 2011.
[16] A. Noual, A. Akjouj, Y. Pennec, J. Gillet, and B. Djafari-Rouhani, "Modeling of two-dimensional nanoscale Y-bent plasmonic waveguides with cavities for demultiplexing of the telecommunication wavelengths," *New J. Phys.*, vol. 11, 2009, Art. no. 103020.
[17] J. Tao, X. Huang, and J. Zhu, "A wavelength demultiplexing structure based on metal–dielectric–metal plasmonic nano-capillary resonators," *Opt. Exp.*, vol. 18, no. 11, pp. 11111–11116, 2010.
[18] J. Tao, X. Huang, J. Chen, and J. Zhu, "All-optical broadband variable optical attenuators and switches in plasmonic teeth waveguides," *Opt. Commun.*, vol. 283, pp. 3536–3539, 2010.
[19] Z. Yu, G. Veronis, S. Fan, and M. Brongersma, "Gain-induced switching in metal-dielectric-metal plasmonic waveguides," *Appl. Phys. Lett.*, vol. 92, 2008, Art. no. 041117.
[20] J. Jacob, A. Babu, G. Mathew, and V. Mathew, "Propagation of surface plasmon polaritons in anisotropic MIM and IMI structures," *Superlattices Microstruct.*, vol. 44, pp. 282–290, 2008.
[21] A. R. Davoyan, I. V. Shadrivov, and Y. S. Kivshar, "Quadratic phase matching in nonlinear plasmonic nanoscale waveguides," *Opt. Exp.*, vol. 17, no. 22, pp. 20063–20068, 2009
[22] F. Lu, G. Li, K. Li, Z. Wang, and A. Xu, "A compact wavelength demultiplexing structure based on arrayed MIM plasmonic nano-disk cavities," *Opt. Commun.*, vol. 285, pp. 5519–5523, 2012.
[23] Q. Li, T. Wang, Y. Su, M. Yan, and M. Qiu, "Coupled mode theory analysis of mode-splitting in coupled cavity system," *Opt. Exp.*, vol. 18, no. 8, pp. 8367–8382, 2010.
[24] F. Zernike, "Refractive indices of ammonium dihydrogen phosphate and potassium dihydrogen phosphate between 2000 Å and 1.5 μ," *J. Opt. Soc. Amer.*, vol. 54, no. 10, pp. 1215–1220, 1964.
[25] P. B. Johnson and R. W. Christy, "Optical constants of the noble metals," *Phys. Rev. B*, vol. 6, pp. 4370–4379, 1972.
[26] S. A. Maier, *Plasmonics: Fundamentals and Applications*. Bath, ME, USA: Springer, 2007.
[27] S. Namba, "Electro-optical effect of zincblende," *J. Opt. Soc. Amer.*, vol. 51, no. 1, pp. 76–79, 1961.
[28] Z. Chen, X. Song, R. Jiao, G. Duan, L. Wang, and L. Yu, "Tunable electromagnetically induced transparency in plasmonic system and its application in nanosensor and spectral splitting," *IEEE Photon. J.*, vol. 7, no. 6, Dec. 2015, Art. no. 4801408.
[29] I. D. Rukhlenko, M. Premaratne, and G. P. Agrawal, "Guided plasmonic modes of anisotropic slot waveguides," *Nanotechnology*, vol. 23, 2012, Art. no. 444006.